



# Additive-free photo-assisted selective partial oxidation at ambient conditions of 5-hydroxymethylfurfural by manganese (IV) oxide nanorods



Dimitrios A. Giannakoudakis<sup>a,b,\*</sup>, Vaishakh Nair<sup>b</sup>, Ayesha Khan<sup>b</sup>, Eleni A. Deliyanni<sup>a</sup>, Juan Carlos Colmenares<sup>b,\*\*</sup>, Konstantinos S. Triantafyllidis<sup>a,\*</sup>

<sup>a</sup> Department of Chemistry, Aristotle University of Thessaloniki, 54124, Thessaloniki, Greece

<sup>b</sup> Institute of Physical Chemistry, Polish Academy of Sciences, Kasprzaka 44/52, 01-224, Warsaw, Poland

## ARTICLE INFO

### Keywords:

Biomass valorization  
Photocatalysis  
Selective oxidation of 5-hydroxymethylfurfural (HMF)  
2,5-diformylfuran (DFF)  
Manganese oxide nanorods

## ABSTRACT

The valorization of natural and renewable resources, like lignocellulosic biomass, towards value-added chemicals by low energy and economically viable processes still remains a global research and technological challenge. 5-hydroxymethylfurfural (HMF) is an important platform chemical that can be easily derived from biomass, and it can be further used as a feedstock for the production of building blocks for polymers or fuels. In this context, the partial oxidation of the hydroxyl group on the HMF molecule leads to the formation of the corresponding aldehyde, 2,5-diformylfuran (DFF), which may find multiple applications in bio-chemical industries. Herein, we present the synthesis and characterization of novel manganese (IV) oxide nanorods as catalyst for the HMF to DFF partial oxidation at ambient conditions. This 1D nanocatalyst operates at low energy light irradiation and without the addition of chemicals (bases or oxidants) as a highly selective photo-assisted catalyst. Under optimized experimental conditions, the HMF conversion was found to be above 99%, while the DFF selectivity was almost 100%. The presence of molecular O<sub>2</sub> played a key role in triggering the selective oxidation, while the use of an aprotic and less polar organic solvent, such as acetonitrile, compared to water, further enhanced the reactivity of the catalyst.

## 1. Introduction

The production of renewable energy has been a major research and technological target over the last decades. Apart from solar, wind and hydro-power, energy and fuels derived from biomass have been also recognized as an important contributor to this effort. EU has set the target of 10% substitution of conventional fuels with biofuels by 2020, and USA of 20% substitution by 2030 [1,2]. In addition to fuels, a wide variety of functional building blocks and platform chemicals, such as 1,4-diacids (succinic, fumaric and malic), 2,5-furan dicarboxylic acid (FDCA), levulinic acid, sugar alcohols (sorbitol, xylitol/arabinitol) and others, can be produced from biomass derived sugars via biological or chemical conversion processes [3–8]. In order to increase the sustainability of biomass valorization, in terms of energy consumption, photocatalysis, as well as other alternative energy source (plasma, microwave, and ultrasound) processes have been explored, in addition to more classical bio- and chemo-catalytic routes, for the conversion of biomass towards added value chemicals [9–14].

Furanics and their derivatives produced from C5 and C6 sugars by

various catalytic processes are amongst the most important biomass related platform chemicals [9,15–18]. A fundamental compound of the furan-family is 5-hydroxymethylfurfural (HMF) produced by the dehydration of glucose/fructose (an intermediate step of glucose isomerization to fructose is usually required) [19–21]. The oxidation product of HMF, i.e. 2,5-furandicarboxylic acid (FDCA), has been utilized as an important renewable building block, substituting terephthalic acid in the production of polyesters, such as polyethylene furanoate (PEF) replacing the petroleum-derived polyethylene terephthalate (PET) in the production of plastics [22–26]. The partial oxidation of HMF leads to the formation of 2,5-diformyl furan (DFF) [27], which is also considered as an important chemical for the synthesis of a wide-range of bio-products, including pharmaceuticals, antifungal agents, furan-based polymers and organic conductors. The current research towards an economically feasible DFF production with low environmental impact, focuses on the use of low cost non-precious/noble metal catalysts, avoidance of hazardous chemicals (bases or organic solvents) and use of mild oxidants (i.e. molecular oxygen), as well as utilization of low temperature/energy consuming processes, such as

\* Corresponding authors at: Department of Chemistry, Aristotle University of Thessaloniki, 54124, Thessaloniki, Greece

\*\* Corresponding author at: Institute of Physical Chemistry, Polish Academy of Sciences, Kasprzaka 44/52, 01-224, Warsaw, Poland.

E-mail addresses: [DaGChem@gmail.com](mailto:DaGChem@gmail.com) (D.A. Giannakoudakis), [jcarloscolmenares@ichf.edu.pl](mailto:jcarloscolmenares@ichf.edu.pl) (J.C. Colmenares), [ktrianta@chem.auth.gr](mailto:ktrianta@chem.auth.gr) (K.S. Triantafyllidis).

sonochemistry and photocatalysis [27–31].

The selective oxidation of biomass derived platform molecules, especially alcohols, aldehydes and ketones, to the corresponding carbonyl or carboxyl counterparts is of a great importance. In order to elucidate the oxidation mechanisms of real biomass process streams, numerous studies have focused on simple model compounds, such as benzyl alcohol or benzaldehyde [32–39]. Manganese oxides have been suggested as excellent candidates in catalytic oxidation of relevant organic molecules [40–43]. The size decrease of MnO<sub>2</sub> porous-spheres was shown to have a positive impact on the catalytic degradation of phenol, while the reduction of Mn oxidation state from +4 to +3 or +2 by annealing had a negative influence [44]. The different possible oxidation states of Mn ions facilitate favorable oxidation-reduction cycles of MnO<sub>2</sub>, thus enhancing its catalytic activity in Advanced Oxidation Processes (AOP) and electron-transfer reactions [10,44–47]. While different commercially available allotropic forms of manganese oxide (MnO<sub>2</sub>, Mn<sub>2</sub>O<sub>3</sub>, and Mn<sub>3</sub>O<sub>4</sub>) showed limited oxidative capability towards HFM, Mn<sub>3</sub>O<sub>4</sub> nanoparticles exhibited enhanced conversion performance of HMF to DFF, at 120 °C under air purging [48]. Yuan et al. reported that un-doped MnO<sub>2</sub> can reach only 2.4% HMF conversion with 89.8% DFF selectivity at 100 °C and 10 bar O<sub>2</sub> pressure in DMF, after 10 h [49]. Additionally, Biswas et al. reported a similarly low conversion of HMF with high DFF selectivity (13% conversion, > 99% DFF selectivity) by mesoporous MnO<sub>x</sub> at higher temperature of 130 °C in DMF [50]. Various other semiconductors and photoactive materials like titanium oxide (TiO<sub>2</sub>), graphitic carbonitride (g-C<sub>3</sub>N<sub>4</sub>), niobium pentoxide (Nb<sub>2</sub>O<sub>5</sub>) etc., were studied as catalyst for the HMF oxidation, but with the simultaneous use of various oxidation agents [39,51–55].

Herein, we report the synthesis of a nanostructured pure MnO<sub>2</sub> and its application as a photo-assisted, additive-free heterogeneous catalyst for the selective partial oxidation of HMF to 2,5-diformylfuran (DFF) under ambient conditions. A wide range of experimental conditions/features like different light sources, temperature, solvents, addition of H<sub>2</sub>O<sub>2</sub> or tuning of pH were investigated. Two homemade photoreactors were designed, assembled and operated for the investigated oxidation reaction. The first one was irradiating light in a wide range of light spectrum (400–1300 nm), but the predominant irradiation was in the visible range (herein referred to as Vis). The second one was a homemade UV emitting (375 nm) LED-based photoreactor, referred to as LED (Fig. 1).

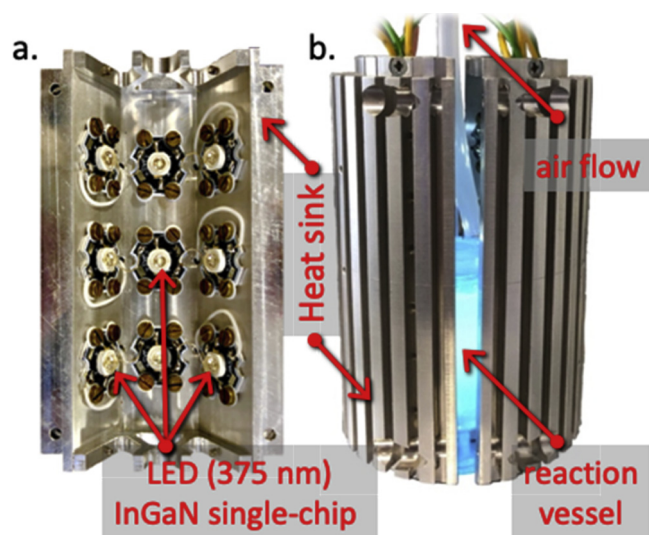


Fig. 1. Photos of the homemade LED photo-reactor; on the left the interior array of the LEDs and on the right the running experimental setup.

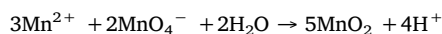
## 2. Experimental

### 2.1. Materials

5-hydroxymethylfurfural (HMF) and 2,5-diformylfuran (DFF) were obtained from Chempur and Acros Organics, respectively. Acetonitrile was purchased from POCH Avantor Performance Materials Poland S.A. Milli Q water was used as the solvent during catalyst synthesis, photocatalytic tests and HPLC mobile phase preparation. The reagents for HPLC analysis were of analytical grade and used without any further purification.

### 2.2. Catalyst synthesis

MnO<sub>2</sub> nanorods (MnO<sub>2</sub>-NRs) were synthesized based on an ultra-slow controlled precipitation procedure. After sonication for 10 min of 50 ml manganese chloride solution (0.3 g/L), a solution of KMnO<sub>4</sub> (3.2 g/400 mL) was added dropwise with a rate of 1 mL/min at room temperature, under continuous stirring, until the solution turned into dark brown, due to the formation of MnO<sub>2</sub> based to the redox reaction [56]:



### 2.3. Materials characterization

High resolution scanning electron microscope (HR-SEM) FEI Nova NanoSEM 450 was used to determine the morphology of the MnO<sub>2</sub> nanorods. The crystalline structure of the catalyst was examined by powder X-ray diffraction (XRD) using a Bruker D8 DISCOVER A25 diffractometer (Bruker Corporation, Billerica, MA, USA), equipped with a vertical-goniometer under theta-theta geometry using Ni filtered CuK<sub>α</sub> (λ = 1.5418 Å) radiation and operated at 40 KeV and 40 mA. N<sub>2</sub> adsorption-desorption experiments at −196 °C were performed on an Automatic Volumetric Sorption Analyzer (Autosorb-1, Quantachrome) for the determination of the surface area (BET method), total pore volume at P/Po = 0.99, micropore volume (t-plot method), and pore size distribution (BJH method) of the samples that were previously out-gassed at 250 °C for 16 h under 5 × 10<sup>−9</sup> Torr vacuum. Diffuse reflectance (DRS) Ultraviolet-Visible spectra were collected by a UV/VIS/NIR spectrophotometer Jasco V-570 (JASCO international Co., Ltd., Hachioji, Tokyo, Japan) equipped with an integrating sphere. Spectralon™ (poly(tetrafluoroethylene)) was used as a reference material for the baseline.

### 2.4. Photocatalytic experiments

The photoreactors were filled with 20 mL of HMF aqueous and/or acetonitrile solution (0.5 mM) and 20 mg of the nanocatalyst (1 g/L). The irradiation protocol was as follows: 40 min in the dark under vigorous stirring (600 rpm) for equilibration in order to determine the possibility of adsorption and/or reactivity even in dark. Then, the light source was applied to the reactor for up to 6 h under continuous stirring (600 rpm). Filtrated solution samples were analyzed after specific time intervals. Tests with hermetically sealed vials and sampling only after 40 min and 6 h were also performed. The headspace of these tests was analyzed by GC.

The solution after the filtration of the suspension at the end of the reaction was analyzed by an energy dispersive X-ray fluorescence (EDXRF) spectrometer (Mini-Pal 4, PANalytical & Co.) with Rh tube and silicon drift detector, for the determination of any possible Mn leaching. The spectra were gathered in air atmosphere (without a filter), at a tube voltage of 30 kV. The acquisition time was 30 s and the current of the tube up to 50 μA.

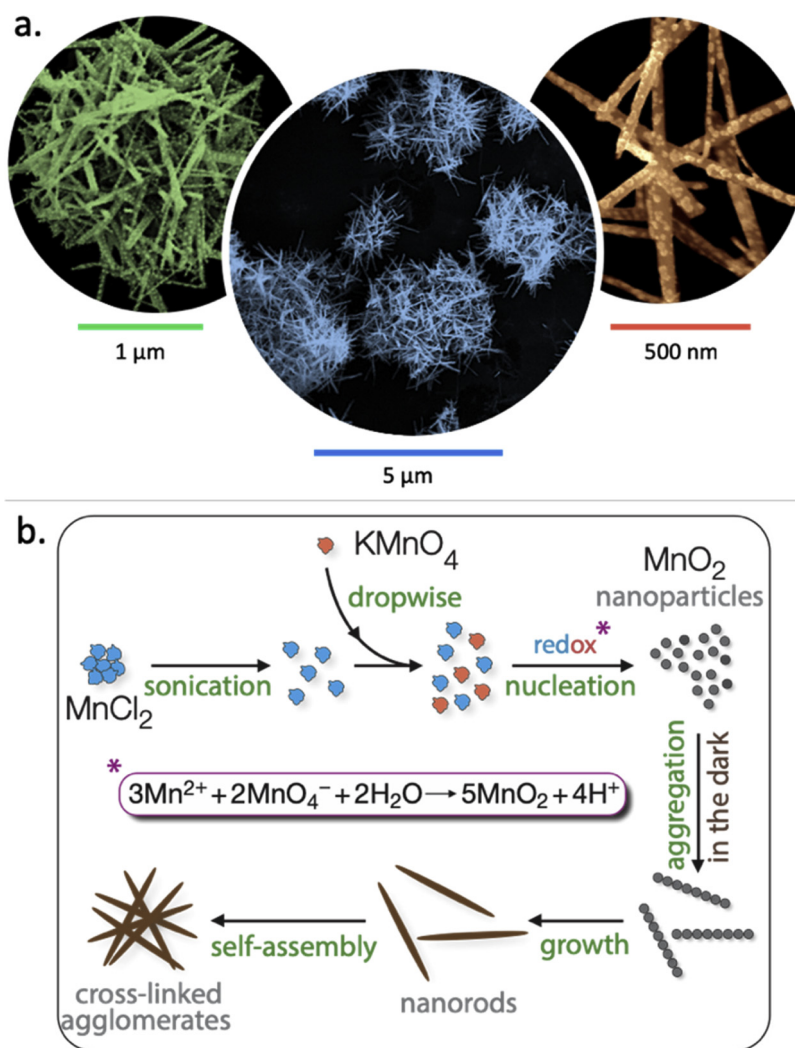


Fig. 2. SEM images (a) and schematic representation of the controlled synthesis of the manganese oxide nanorods (b).

## 2.5. Photoreactors and light sources

### 2.5.1. Visible light (Vis)

A 150 W 3200 K Fiber Optic Illuminator from Spectra Laser served as the source of the visible and infrared light driven experiments. The lamp is equipped with a dichroic filter (Hot Mirror) in order for the undesired heat produced from the halogen to be eliminated. The spectrum of the Vis-IR ranged from 400 nm (3.1 eV) to 1300 nm (0.95 eV), with the predominant energy to be in the visible range, and it is referred to as Vis. A flexible fiber bundle with a diameter of 95 cm was used for the irradiation of the reactor with the Vis light, as can be seen in the schematic illustration of Figure S-1 (Supporting Information). The power of VIS light behind the optical fiber is about 1.2 W, while the maximum intensity is about 430,000 lx. The intensity of the halogen source was regulated by a potentiometer at around 70%.

### 2.5.2. UV – LED system

The homemade LED photoreactor can be seen in the photos of Fig. 1. It consists of two heat sinks. There are nine InGaN based single chip LEDs in the interior part of each piece, with a peak wavelength at 375 nm. The current was 0.3 mA. The control of the temperature inside the reactor (in the range of 26–39 °C) was achieved by air purging inside the reactor. The absence of air flow inside the LED system led to an increase of the temperature, and as a direct consequence to an increment of the suspension temperature during the reaction. Without cooling of the interior of the system, the temperatures found to be

between 38 and 40 °C. With air purging (Figure S-2, Supporting Information), the temperature was controlled at around 26 °C. For the experiments performed in the dark, the reaction vials were covered with aluminum foil.

## 2.6. Products analysis

An HPLC (Acquity Arc Waters) equipped with a 2998 Photodiode Array detector using a mixture of Acetonitrile and Mili-Q water as mobile phase was used for the analysis of the filtrated solutions. HMF and DFF were well separated by a C18 Thermo scientific column (250 x 4.6 mm). The compounds were detected by a UV detector at 270 nm. The mobile phase was composed of acetonitrile and Mili-Q water with 55:45 v/v ratio. The flow rate was set at 1.0 mL/min and the temperature of column oven was kept at 25 °C. The concentrations of HMF and DFF were determined based on the HPLC chromatograms (two well separated peaks for HMF and DFF at retention time of 2.69 and 3.65 min, respectively) and the calibration curves.

## 2.7. Calculation of HMF conversion - products yield and selectivity - carbon balance

The initial concentration of HMF ( $C_{HMF,in}$ ), the final concentration of HMF ( $C_{HMF,f}$ ), the concentration of DFF ( $C_{DFF}$ ) and the concentration of FDCA ( $C_{FDCA}$ ) were determined by the HPLC analyses. HMF conversion (%), DFF Yield (%), FDCA Yield (%), DFF selectivity (%), and carbon

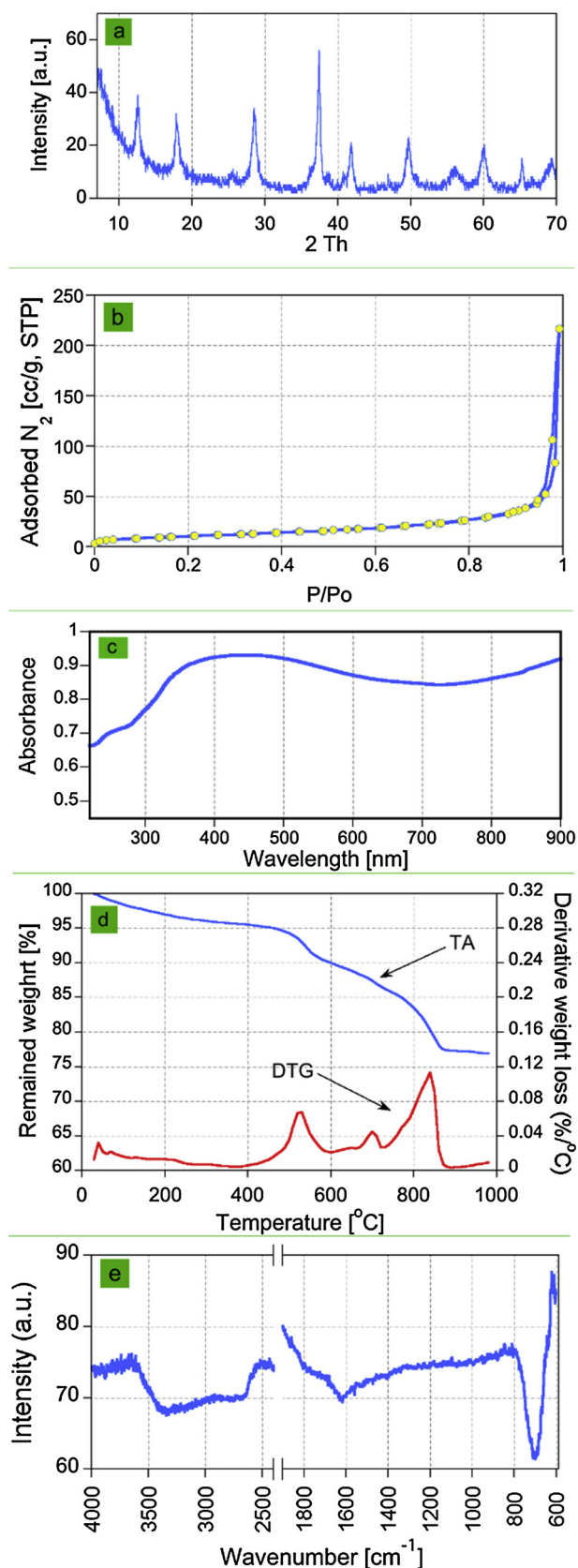


Fig. 3. The XRD pattern (a), N<sub>2</sub> adsorption-desorption isotherms at -196 °C (b), diffuse reflectance UV-vis absorbance spectrum (c), TGA and DTG curves (d), and FTIR spectrum (e) of the initial MnO<sub>2</sub>-NRs.

balance (%) were estimated by using the following equations:

$$\text{HMF conversion (\%)} = 100 * (C_{\text{HMF,in}} - C_{\text{HMF,f}}) / C_{\text{HMF,in}}$$

$$\text{DFF Yield (\%)} = 100 * C_{\text{DFF}} / C_{\text{HMF,in}}$$

$$\text{FDCA Yield (\%)} = 100 * C_{\text{FDCA}} / C_{\text{HMF,in}}$$

$$\text{DFF Selectivity (\%)} = 100 * C_{\text{DFF}} / (C_{\text{HMF,in}} - C_{\text{HMF,f}})$$

$$\text{Carbon Balance (\%)} = 100 * (C_{\text{HMF,f}} + C_{\text{DFF}} + C_{\text{FDCA}}) / C_{\text{HMF,in}}$$

### 3. Results and discussion

#### 3.1. Catalyst characterization

The morphological analysis of the prepared MnO<sub>2</sub> by SEM (Fig. 2a) revealed that the herein followed controlled precipitation procedure (Fig. 2b) resulted in the formation of spherical aggregates with size of ca. 1–5 μm, consisting of cross-linked uniform nanorods (NRs) with dimensions ranging from 10 to 55 nm in diameter and length of 150 nm to 1.5 μm. The XRD pattern (Fig. 3a) matches to the body-centered tetragonal α-MnO<sub>2</sub> (JCPDS card, no. 44-0141) [57,58]. The key morphology modulation synthetic feature is the ultra-slow addition of KMnO<sub>4</sub>, that induces the oxidation of Mn<sup>2+</sup> to Mn<sup>4+</sup> and favors the nucleation of MnO<sub>2</sub> nanoparticles in the dark, as shown in Fig. 2b. These nanoparticles aggregate and grow as nanorods which are self-assembled to the obtained structures.

The nitrogen physisorption experiments revealed a *Type II* isotherm (Fig. 3b) without hysteresis loop, characteristic of nonporous or macroporous materials [59]. The BET surface area was 38.5 m<sup>2</sup>/g and the total pore volume (at P/P<sub>0</sub> ~ 0.99) 0.336 cm<sup>3</sup>/g. The interstitial spaces between the aggregated/packed nanorods are responsible for the formed porosity, as was reported for other nanomaterials with similar morphology [60,61]. Furthermore, the remarkable increase of sorbed N<sub>2</sub> at P/P<sub>0</sub> 0.95–0.99, indicate the very high external surface, in agreement with the morphology of the individual nanorods. Diffuse reflectance spectroscopy (DRS) revealed strong light absorption in the whole range of UV-vis (Fig. 3c), in accordance with the dark brown color of the material. The absence of a clear estimated band gap indicates that the material cannot be considered as a typical semiconductor [46]. The TGA and DTG profiles of the fresh MnO<sub>2</sub>-NRs are shown in Fig. 3d. The weight loss below 100 °C is due to physisorbed water [62]. The two DTG peaks in this temperature range suggest the removal of water molecules initially from the external surface, followed by those from the interstitial spaces [60,61]. The three major weight losses above 400 °C with DTG maxima at 530, 710, and 840 °C, can be linked to the phase transformations of MnO<sub>2</sub> to Mn<sub>2</sub>O<sub>3</sub>, Mn<sub>3</sub>O<sub>4</sub>, and Mn<sub>x</sub>, respectively, and are in an agreement with the reported in the literature phase transformations of MnO<sub>2</sub> upon calcination [44,63,64]. The FTIR spectrum of the initial sample (Fig. 3e) showed two characteristic strong and wide bands with centers at 1625 and 707 cm<sup>-1</sup> which can be assigned to the Mn-O stretching modes [48]. The presence of hydrogen bonded water moieties can also be attributed to the wide and intense band between 2800 to 3600 cm<sup>-1</sup>.

#### 3.2. Catalytic results - effect of different light wavelengths

With regard to the targeted reaction, the partial oxidation of HMF, the aim was to evaluate the effect of visible light versus UV irradiation in different solvents, with or without an oxidative agent and/or slightly higher temperature than room temperature. Water and acetonitrile (AcN) were used as solvents, pure, as a mixture (50:50 v/v) or with the addition of hydrogen peroxide. AcN was chosen in order to check if the alteration of the oxygen solubility, pH, and/or polarity of the solvent play a role in HMF conversion and DFF selectivity.

In the case of visible light-driven tests, when water was the solvent,

pure (pH = 7 ± 0.3) or in mixture with AcN (pH = 7.4 ± 0.3), the conversion of HMF was limited. On the contrary, when pure AcN was used (pH = 8 ± 0.3), the conversion was 81%, with 76% yield and 93% selectivity to 2,5-diformyl furan (DFF). These differences can be due to the occupation/hindrance/blockage of the active surface functional groups by water molecules, probably via H-bonds, leading to a complete coating of the nanorods' outer active surface and/or to the significant lower O<sub>2</sub> solubility in water by around five folds compared to acetonitrile (8.1 mM) [65–69]. These effects can explain the negative impact on conversion (< 5%) upon addition of aqueous hydrogen peroxide solution in acetonitrile. In order to conclude if the superior catalytic ability in acetonitrile is assigned to the increased pH or to the different polarity of the aprotic solvent, tests at pH = 10 in aqueous solution (NaOH addition) were performed and the conversion to DFF was found negligible.

### 3.3. Evaluation of reactivity in the dark

It should be pointed out that the MnO<sub>2</sub>-NRs showed an elevated conversion in AcN even during the equilibration in the dark. In order to elucidate this aspect, catalytic tests were also performed in the dark and all the related data are presented in Table 1, Fig. 4, and Figure S-3 (Supporting Information). The results revealed that the nanorods can selectively oxidize HMF to DFF even in the dark at 24 °C, as a result of the high surface reactivity, but the conversion and selectivity were 63 and 92%, respectively. Considering these values, it can be concluded that the experimental conditions and the nature of the MnO<sub>2</sub>-NRs favor exclusively the partial oxidation of HMF as a result of the high surface reactivity of nanorods. Taking into account also that no other products were detected, while the carbon balance (CC) was 95%, we can consider adsorption phenomena as low and insignificant. Increment of reaction temperature to 37 °C, led to a higher by only 5% conversion, compared to 24 °C. The detection of 2,5-furandicarboxylic acid, FDCA, (1% yield) can explain the observed lower selectivity, since a minimal portion of DFF is further oxidized by some thermally activated defects (like Mn<sub>3</sub>O<sub>4</sub>), that can promote alternative reaction pathways. Based on the above, the increase of temperature in the dark has a limited effect.

### 3.4. Catalysis under UV light irradiation

As can be observed in Fig. 4, the UV-irradiation led to an improved conversion (89%, a-RT-UV), which is higher by 56 and 10% compared to the reaction in the dark (a-RT-d) and under Vis-irradiation (a-RT-Vis), respectively, at similar temperature. The photolysis test showed that the UV-irradiation can also lead to transformation and/or mineralization of HMF to undesirable/undetected products (carbon balance 83.9%). It is also vital that the minimal HMF photolysis at 26 °C (16% conversion) was not accompanied with DFF formation. On the contrary, the presence of MnO<sub>2</sub>-NRs overcomes the unselective-photolysis of

HMF under UV-irradiation, leading to selective oxidation to DFF (DFF selective 94%). The carbon balance of 95% can be linked to the minimal adsorption phenomena as discussed above. It can thus be suggested that the presence of MnO<sub>2</sub> nanorods favors the partial oxidation of HMF to DFF instead of being decomposed.

Considering the above, it was established that the light irradiation has a positive impact on the oxidative performance. This can be attributed to the photoreactivity excitation and to the temperature increase of NRs surface or/and of the suspension due to light absorption. The synergistic effect by combining two processes, thermo- and photocatalysis, can lead to process intensification for various environmental and energy applications [70]. It is worth to mention that the temperature inside the reactor was higher in the presence of the catalyst by 2 °C compared to the photolysis test (no catalyst) under the same experimental conditions, as a result of the physical properties of the nanorods (dark brown color). In order to check the temperature effect, tests were performed at barely higher temperature of 38 °C. HMF photolysis was increased slightly, from 16% (27 °C) to 18.6% (38 °C), but the carbon balance decreased. For MnO<sub>2</sub>-NRs, increase of the temperature by 13 °C in the dark has accompanied with a 9% conversion enhancement, while the selectivity was affected negatively by 4%. For UV-light assisted tests, the increase of the temperature from 28 to 39 °C was supplemented with improved conversion, from 89 to 99%. The DFF selectivity and yield were also enhanced from 94 and 84%, respectively, to 100 and 98%, while the carbon balance was almost 100%.

UV-irradiation tests with the MnO<sub>2</sub>-NRs at 39 °C were performed also in aqueous suspensions. The observed conversion of 15% at 39 °C was dramatically lower compared to the use of acetonitrile as solvent (99%) (Table 1). When comparing UV versus Vis light irradiation using water as solvent, both HMF conversion and DFF selectivity were higher in the first case. It is also worth mentioning that FDCA was formed (6% yield), suggesting the possibility of water acting as source of reactive oxygen species, responsible for the oxidation of –CHO to –COOH.

### 3.5. Comparison with other reported Mn-based catalysts

A literature survey for Mn<sub>x</sub>O<sub>y</sub> materials as HMF oxidation catalysts is presented in Table 2; two specific examples using MnO<sub>2</sub> are also shown in Fig. 4 [9,48,50]. All the reported studies were performed at relatively high temperatures (90–120 °C) and with air/O<sub>2</sub> purging. Commercial Mn<sub>x</sub>O<sub>y</sub> revealed poor catalytic performance (6.5% conversion with MnO<sub>2</sub>). Nanostructured-Mn<sub>3</sub>O<sub>4</sub> showed full conversion, but at 120 °C and with 83% selectivity [48]. Porous MnO<sub>2</sub> molecular-sieve presented 30% conversion at 90 °C [9]. The MnO<sub>2</sub>-NRs presented in our work reached almost 100% HMF conversion and selectivity to DFF, at only 39 °C without any additives such as oxidants and/or air purging.

**Table 1**  
Catalytic results of the HMF oxidation under different conditions.

Exp. Abbrev.	Material	solvent	Light source	Temp.	C <sub>HMF,eq</sub> (mM)	C <sub>HMF,f</sub> (mM)	HMF Conv. (%)	C <sub>DFF</sub> (mM)	C <sub>FDCA</sub> (mM)	DFF Select. (%)	DFF yield (%)	FDCA yield (%)	Carbon balance
w-RT-Vis	MnO <sub>2</sub> -NRs	H <sub>2</sub> O	VL	29	0.491	0.487	3	0.005	0.000	38	1.0	0.0	98
a-RT-Vis	MnO <sub>2</sub> -NRs	AcN	VL	28	0.458	0.084	83	0.380	0.000	93	76	0.0	93
a-RT-d	MnO <sub>2</sub> -NRs	AcN	–	24	0.459	0.182	63	0.294	0.000	92	59	0.0	95
a-IT-d	MnO <sub>2</sub> -NRs	AcN	–	37*	0.444	0.169	66	0.309	0.005	93	62	1.0	96
a-RT-PL	–	AcN	LED	26	0.499	0.420	16	0.001	0.000	1	0	0	84
a-IT-PL	–	AcN	LED	38	0.500	0.407	19	0.000	0.000	0.0	0	0	81
a-RT-UV	MnO <sub>2</sub> -NRs	AcN	LED	28	0.443	0.054	89	0.421	0.000	94	84	0.0	95
a-IT-UV	MnO <sub>2</sub> -NRs	AcN	LED	39	0.439	0.007*	99	0.491	0.001	~100	98	0.2	100
w-IT-UV	MnO <sub>2</sub> -NRs	H <sub>2</sub> O	LED	39	0.493	0.423*	15	0.046	0.029	61	9	5.8	100

\*Reaction conditions: initial HMF 0.5 mM (20 mL), 1 g/L photocatalyst (20 mg), reaction time: 40 min equilibration in the dark followed by 6 h of reaction under different light conditions; w: water, a: acetonitrile, RT: 24–29 °C, IT: 37–39 °C, d: in the dark, Vis: visible light, UV: UV light from LED system (365 nm), PL: photolysis tests.

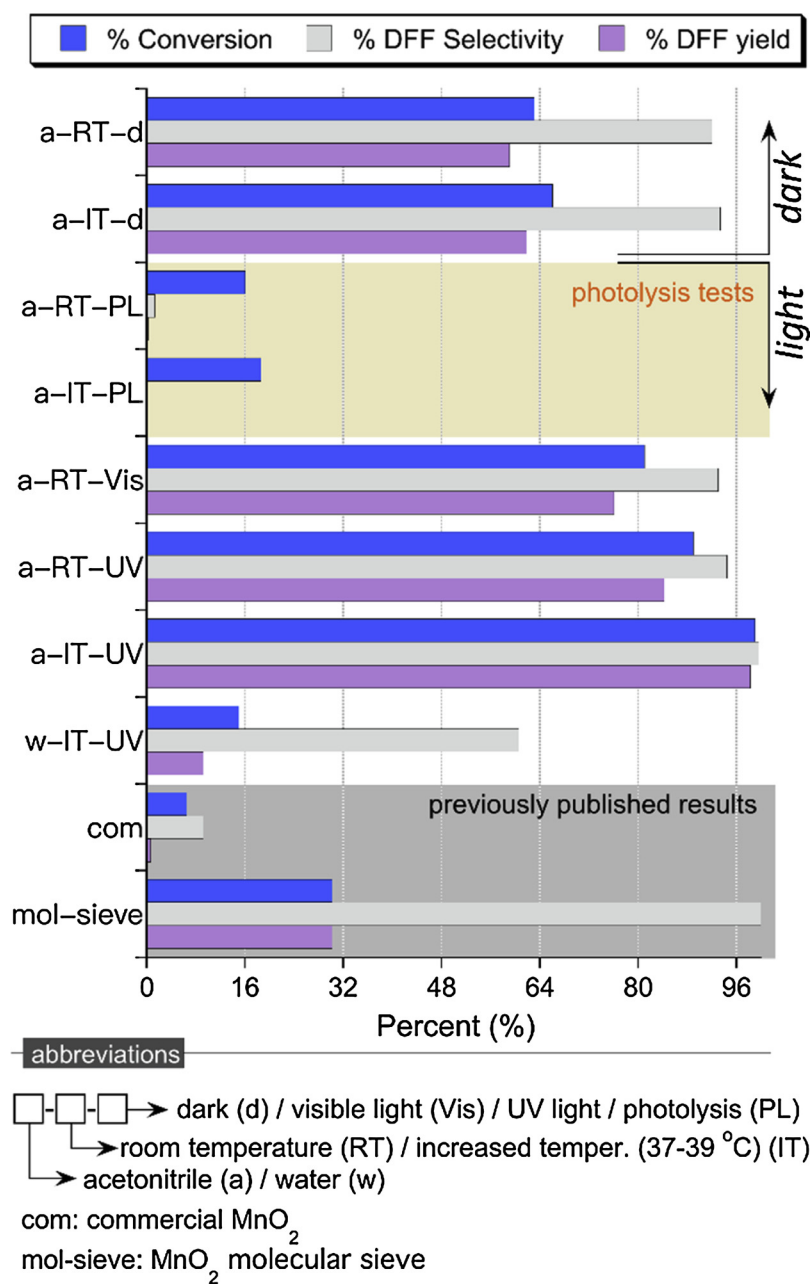


Fig. 4. HMF conversion, DFF yield and DFF selectivity under different reaction conditions by the use of the MnO<sub>2</sub>-NRs; previous literature results with MnO<sub>2</sub> materials are included for comparison [9,48].

Table 2

Comparison of the herein reported HMF oxidation results with other manganese-based catalysts.

Material	Solvent	Reaction conditions	Duration (h)	HMF conversion (%)	DFF yield/selectivity (%)	Ref.
MnO <sub>2</sub> commercial	DMF	120 °C, air purging	12	6.5	0.6/9.2	[48]
Mn <sub>2</sub> O <sub>3</sub> commercial	DMF	120 °C, air purging	12	7.7	2.3/29.9	[48]
Mn <sub>3</sub> O <sub>4</sub> commercial	DMF	120 °C, air purging	12	23.4	17.8/76.1	[48]
Mn <sub>3</sub> O <sub>4</sub> nanoparticles	DMF	120 °C, air purging	4	100	83.2/83.2	[48]
Mesoporous MnO <sub>x</sub>	DMF	130 °C, under air	4	13	- / > 99	[50]
MnO <sub>2</sub> molecular sieve	TOL	90 °C, O <sub>2</sub> purging	12	30.2	-/100	[9]
Mn <sub>3</sub> O <sub>4</sub> molecular sieve	TOL	90 °C, O <sub>2</sub> purging	12	33.4	-/100	[9]
MnO <sub>2</sub> nanorods	ACN	24 °C, no light, no additive	4	63	59/92	This work
MnO <sub>2</sub> nanorods	ACN	28 °C, UV light, no additive	4	89	62/93	This work
MnO <sub>2</sub> nanorods	ACN	37 °C, no light, no additive	4	66	62/93	This work
MnO <sub>2</sub> nanorods	ACN	39 °C, UV light, no additive	4	99	99/100	This work

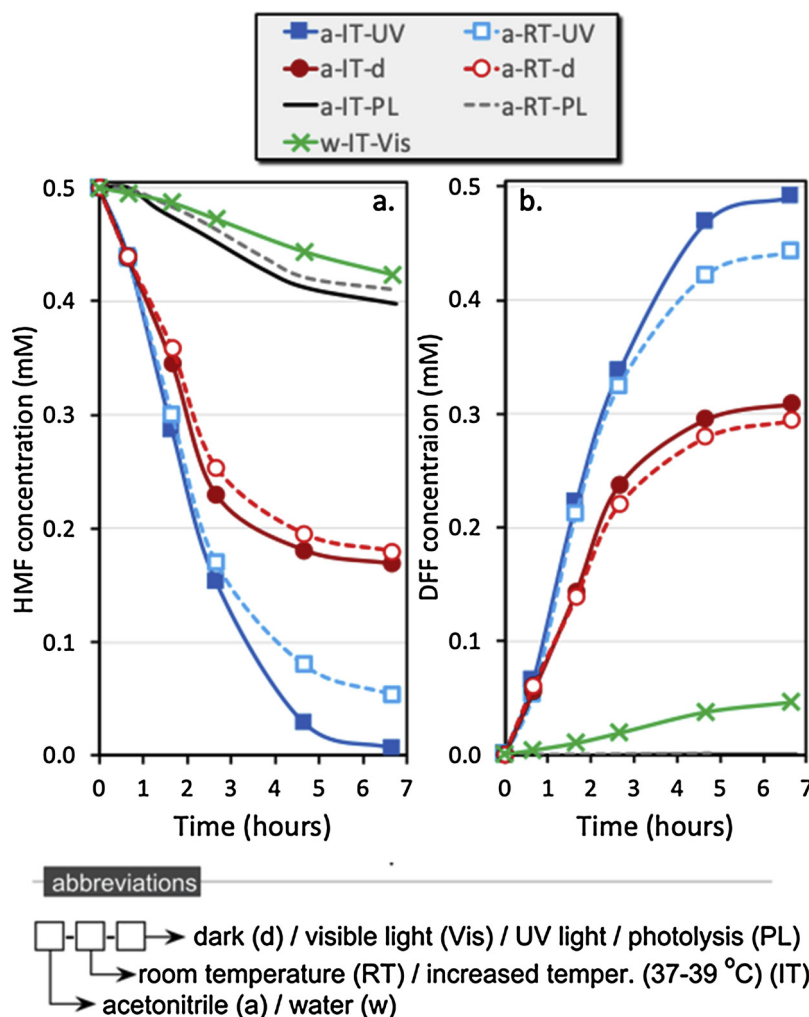


Fig. 5. The evolution of HMF and DFF concentrations with time, under different reaction conditions.

### 3.6. Evaluation of the reaction kinetics

It was also crucial to explore whether the light irradiation had a positive influence on the oxidation kinetics. The evolution of the HMF and DFF concentration is shown in Fig. 5a and 5b. It can be observed that the curves of HMF conversion and DFF formation presented a plateau after 5 h of irradiation, due to the depletion of the reactive centers, owing to various possible reasons, that will be analyzed later. The most important outcome arises from the comparison of the slopes for UV-light exposure and in the dark at 38–39 °C. The light exposure led to an enhanced HMF conversion initial reaction rate of 0.120 mmol/min (0.075 mmol/min in the dark), without a compromise on the selectivity. For the tests performed at lower temperatures (24–29 °C), the initial conversion reaction rates had similar values with the ones at 38–39 °C. This finding further supports that light irradiation has also a positive impact on the oxidation kinetics of HMF towards DFF. It is important to point out that the HMF photolysis test was not accompanied with DFF formation, and after 5 h the decomposition rate of HMF was decreased. When the reaction was performed in water at 39 °C, the conversion rate was dramatically lower compared to AcN, and a plateau was not reached. This further verifies the hindered (by water molecules) interaction of HMF molecules with the active MnO<sub>2</sub> surface-sites. The conversion in water at lower temperature or in the dark was almost negligible.

### 3.7. Characterization of the spent catalyst

Comprehensive characterization of the spent catalyst samples was also performed and the obtained data are presented in the Supporting Information. In summary, the structural and surface characteristics of the MnO<sub>2</sub>-NRs were not altered significantly. The detection of low intensity XRD reflections (Figure S-4) assigned to Mn<sub>2</sub>O<sub>3</sub> or MnO revealed a limited reduction of MnO<sub>2</sub>, possibly at defect sites. These Mn<sub>2</sub>O<sub>3</sub> sites can be also responsible for the observed limited adsorption of organics and/or the non-selective conversion of HMF. The additional weight loss step of ca. 4 wt.% in the TGA profile of the used catalyst (Figure S-5), at about 100–300 °C (with a DTG maximum at about 250 °C) can be attributed to the decomposition/desorption of sorbed small amounts of HMF and/or DFF, in accordance to the detection of specific IR bands at 1653 and 1397 cm<sup>-1</sup> related to the sorbed HMF/DFF (Fig. S-6). Still, the very high (ca. > 95% carbon balance) in all the catalytic experiments indicate the low extent of HMF/DFF sorption on the MnO<sub>2</sub>-NRs, which is very critical in order to maximize the productivity of the desired product. Analysis of the spent catalyst by SEM imaging (Fig. S-7) did not reveal any morphology alteration of the nanorods even after 7 h of operation. The stability of the catalyst was also investigated by checking the Mn leaching after 6 h using XRF analysis (Fig. S-8), revealing only the presence of Mn traces in the reaction solution.

### 3.8. Suggested reaction mechanism for the selective oxidation of HMF

The catalytic reactivity of MnO<sub>2</sub> in the decomposition of organic

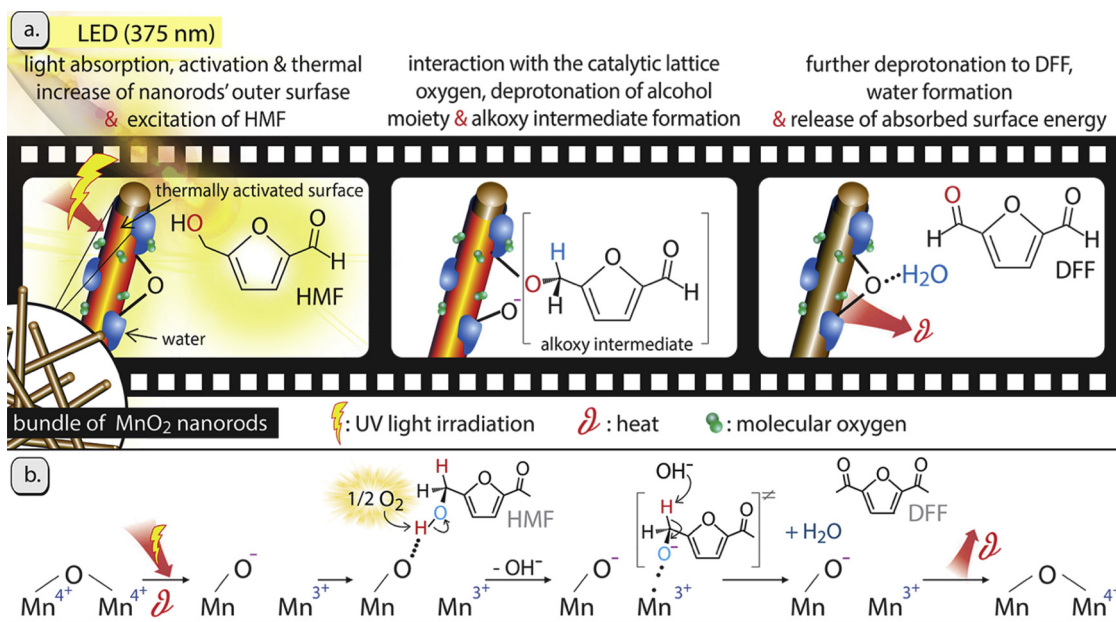


Fig. 6. Illustrated representation of the light effect and the involved oxidation mechanism of HMF over MnO<sub>2</sub>-NRs.

compounds or for water splitting was rationalized in previous works on the basis of the redox cycle between Mn<sup>4+</sup> and Mn<sup>3+</sup> and the contribution of O<sub>2</sub> [9,71]. MnO<sub>2</sub> has a lower covalence band potential compared to the redox potential for O<sub>2</sub>/O<sub>2</sub><sup>-</sup> [71], suggesting that the charge transfer during the catalytic transformations follows the Mn<sup>4+</sup>/Mn<sup>3+</sup> redox cycle. The partial oxidation to DFF does not require the incorporation of oxygen atoms on the HMF molecule, but the removal of two hydrogen atoms by the cleavage of one O–H and one C–H bond. It should be pointed out that various MnOx based catalysts in previous works, had not shown the capability to form oxygen containing free radicals without the addition of a reagent like H<sub>2</sub>O<sub>2</sub> [50,57,72]. In our case, the mild heat and light promoted the activation of the nanorods' lattice oxygens and increased the outer nanorods' surface temperature [73]. Additionally, the energy state of the C–H and O–H bonds of HMF's hydroxyl group was also increased [73,74]. This leads to the adsorption of HMF via the –C–OH moiety on the O<sup>-</sup> sites (deprotonated Brønsted sites) [73,75,76]. This, along with the simultaneous involvement of molecular oxygen, favors the alcohol deprotonation, via the formation of a transient alkoxy intermediate [40,50,72]. The role of molecular oxygen is to attack the hydrogen of the HMF's hydroxyl group (deprotonation), forming a hydroxide ion, which in turn attacks a hydrogen from the alkoxy intermediate, leading to the desorption of the organic molecule from the surface as DFF with the simultaneous formation of water, followed by the re-oxidation of Mn<sup>3+</sup> to Mn<sup>4+</sup>. Similar pathways were previously suggested on the basis of isotopic labeling studies, showing that the molecular oxygen is not incorporated into the HMF oxidation products [74,77].

The detection of limited Mn<sub>2</sub>O<sub>3</sub> phase on the spent catalyst samples by XRD supports the formation of the Mn<sup>3+</sup> intermediate state. Analogous mechanism was proposed for the oxidation of alcohols by Mn<sub>3</sub>O<sub>4</sub>, but at 90 °C [9]. When tests were performed with degassed acetonitrile, the oxidation extent and rate were found to be lower compared to not-degassed solvent, a fact that sets the involvement of O<sub>2</sub> as the rate determining step. It should be highlighted that the maximum dissolved concentration of oxygen in acetonitrile (8.1 mM at 25 °C) [69] is quantitatively enough for the partial oxidation.

In order to verify the important role of oxygen, tests were performed in hermetically sealed vials. These experiments provided the option to analyze additionally the headspace of the reactor by GC and to conclude if molecular (gaseous) hydrogen was formed via the deprotonation of HMF. Interestingly, the conversion of HMF with MnO<sub>2</sub>-NRs (in

acetonitrile at 39 °C) after 6 h was only 21%, and the selectivity to DFF 67%. Hydrogen was not detected in the headspace of the vials, suggesting that the deprotonation is facilitated by the formation of water. The detection of small traces of CO<sub>x</sub>, suggests that without the presence of O<sub>2</sub>, the reaction occurs by the cleavage of a C–C bond of HMF. The formation of water molecules sterically hinders/blocks the catalytic surface-centers, by forming hydrogen bonds, resulting in an activity decrement as revealed from the gradual decrease of conversion as the reaction continued. The use of an aprotic and less polar organic solvent compared to water, as AcN, results in a positive impact on the rate determining step, by a higher O<sub>2</sub> solubility and promoting oxygen molecules to be entrapped in the interface between AcN and the nanorods outer surface. If the water was in excess, another negative impact would be the possible formation of hydrogen bonds with the hydroxyl group of HMF, thus inhibiting its direct interaction with the catalyst's surface (lattice oxygens). All suggested/involved mechanisms are summarized in Fig. 6.

#### 4. Conclusions

The combination of nanostructured active MnO<sub>2</sub> nanorods with low energy light emission can boost a versatile environmentally-friendly heterogeneous and additive-free (oxidants and/or air purging) catalytic HMF-to-DFF oxidation at ambient conditions. A slight increase of the temperature as a result of the light irradiation can rise further the catalytic efficiency, but the light irradiation itself plays a more important role than the temperature increment. The latter acts synergistically to the irradiation by enhancing the reaction rate. The UV light was found to have a more pronounced positive impact compared to visible light. The absence of water is also crucial since water molecules can hinder HMF interaction with the active catalytic centers. Another vital outcome is that the presence of molecular oxygen is a mandatory parameter for the proposed mechanism. Under UV exposure at 39 °C, HMF conversion, DFF selectivity, and carbon balance was almost 100%. There are no reports up to now and to the best of our knowledge with so elevated additive-free and selective performance of partial HMF oxidation at ambient conditions. Since the oxidative capability is negatively affected by the formed water moieties that were retained on the outer phase of the nanorods, their removal by, for example, ultrasounds during the reaction is worth to be studied. The synthesis of nanostructured active catalyst with tailored surface redox properties is a key

point in order to achieve supreme and selective conversion even with the use of low-energy LED systems, following the principals of Green Chemistry. Finally, the herein used low-energy photoreactors are suitable for continue-flow setups.

## Acknowledgements

DAG would like to thank the COST Action FP1306 for the support through a Short Term Scientific Mission. This publication is part of a project that has received funding from the European Union's Horizon 2020 research and innovation program under the Marie Skłodowska-Curie grant agreement No. 711859 and Scientific work funded from the financial resources for science in the years 2017-2021 awarded by the Polish Ministry of Science and Higher Education for the implementation of an international co-financed project.

## Appendix A. Supplementary data

Supplementary material related to this article can be found, in the online version, at doi:<https://doi.org/10.1016/j.apcatb.2019.117803>.

## References

- [1] European parliament and the council of the European union, directive 2009/28/EC of the European parliament and of the council of 23 April 2009, Off. J. Eur. Union 140 (2009) 16–62, <https://doi.org/10.3000/17252555.L.2009.140.eng>.
- [2] D.C.E.R.D. Perlack, L.L. Wright, A. Turhollow, R.L. Graham, B. Stokes, Biomass As Feedstock for a Bioenergy and Bioproducts Industry: The Technical Feasibility of a Billion-ton Annual Supply, Oak Ridge National Laboratory, Oak Ridge, TN, 2005 37831.
- [3] T. Werpy, G. Petersen, Top Value Added Chemicals From Biomass Volume I — Results of Screening for Potential Candidates From Sugars and Synthesis Gas Top Value Added Chemicals From Biomass Volume I: Results of Screening for Potential Candidates, (2004), <https://doi.org/10.2172/15008859>.
- [4] J.J. Bozell, G.R. Petersen, Technology development for the production of biobased products from biorefinery carbohydrates - the US Department of Energy's "top 10" revisited, Green Chem. 12 (2010) 539–554, <https://doi.org/10.1039/b922014c>.
- [5] R. Luque, C. Len, K. Triantafyllidis, Editorial: nano-(Bio) catalysis in lignocellulosic biomass valorization, Front. Chem. 6 (2018) 1–3, <https://doi.org/10.3389/fchem.2018.00577>.
- [6] G. Fiorentino, M. Ripa, S. Ulgiati, Chemicals from biomass: technological versus environmental feasibility. A review, Biofuels Bioprod. Biorefin. 11 (2017) 195–214, <https://doi.org/10.1002/bbb.1729>.
- [7] L. Wu, T. Moteki, A.A. Gokhale, D.W. Flaherty, F.D. Toste, Production of fuels and chemicals from biomass: condensation reactions and beyond, Chem 1 (2016) 32–58, <https://doi.org/10.1016/j.chempr.2016.05.002>.
- [8] M.J. Gilkey, B. Xu, Heterogeneous catalytic transfer hydrogenation as an effective pathway in biomass upgrading, ACS Catal. 6 (2016) 1420–1436, <https://doi.org/10.1021/acscatal.5b02171>.
- [9] B. Sarmah, B. Satpati, R. Srivastava, Selective oxidation of biomass-derived alcohols and aromatic and aliphatic alcohols to aldehydes with O<sub>2</sub>/air using a RuO<sub>2</sub>-supported Mn<sub>3</sub>O<sub>4</sub> catalyst, ACS Omega 3 (2018) 7944–7954, <https://doi.org/10.1021/acsomega.8b01009>.
- [10] G. Chatel, S. Valange, R. Behling, J.C. Colmenares, A combined approach using sonochemistry and photocatalysis: how to apply sonophotocatalysis for biomass conversion? ChemCatChem 9 (2017) 2615–2621, <https://doi.org/10.1002/cctc.201700297>.
- [11] J.C. Colmenares, R. Luque, Heterogeneous photocatalytic nanomaterials: prospects and challenges in selective transformations of biomass-derived compounds, Chem. Soc. Rev. 43 (2014) 765–778, <https://doi.org/10.1039/c3cs60262a>.
- [12] L.I. Granone, F. Sieland, N. Zheng, R. Dillert, D.W. Bahnemann, Photocatalytic conversion of biomass into valuable products: a meaningful approach? Green Chem. 20 (2018) 1169–1192, <https://doi.org/10.1039/c7gc03522e>.
- [13] S.H. Li, S. Liu, J.C. Colmenares, Y.J. Xu, A sustainable approach for lignin valorization by heterogeneous photocatalysis, Green Chem. 18 (2016) 594–607, <https://doi.org/10.1039/c5gc02109j>.
- [14] S. Yurdakal, G. Palmisano, V. Loddò, O. Alagöz, V. Augugliaro, L. Palmisano, Selective photocatalytic oxidation of 4-substituted aromatic alcohols in water with rutile TiO<sub>2</sub> prepared at room temperature, Green Chem. 11 (2009) 510–516, <https://doi.org/10.1039/b819862d>.
- [15] L. Hu, J. Xu, S. Zhou, A. He, X. Tang, L. Lin, J. Xu, Y. Zhao, Catalytic advances in the production and application of biomass-derived 2,5-Dihydroxymethylfuran, ACS Catal. 8 (2018) 2959–2980, <https://doi.org/10.1021/acscatal.7b03530>.
- [16] W.J. Liu, L. Dang, Z. Xu, H.Q. Yu, S. Jin, G.W. Huber, Electrochemical oxidation of 5-hydroxymethylfurfural with NiFe layered double hydroxide (LDH) nanosheet catalysts, ACS Catal. 8 (2018) 5533–5541, <https://doi.org/10.1021/acscatal.8b01017>.
- [17] J. Chen, R. Liu, Y. Guo, L. Chen, H. Gao, Selective hydrogenation of biomass-based 5-hydroxymethylfurfural over catalyst of palladium immobilized on amine-functionalized metal-organic frameworks, ACS Catal. 5 (2015) 722–733, <https://doi.org/10.1021/cs5012926>.
- [18] Y. Wang, P. Prinsen, K.S. Triantafyllidis, S.A. Karakoulia, P.N. Trikalitis, A. Yezep, C. Len, R. Luque, Comparative study of supported monometallic catalysts in the liquid-phase hydrogenation of furfural: batch versus continuous flow, ACS Sustain. Chem. Eng. 6 (2018) 9831–9844, <https://doi.org/10.1021/acssuschemeng.8b00984>.
- [19] I.K.M. Yu, D.C.W. Tsang, Conversion of biomass to hydroxymethylfurfural: a review of catalytic systems and underlying mechanisms, Bioresour. Technol. 238 (2017) 716–732, <https://doi.org/10.1016/j.biortech.2017.04.026>.
- [20] B. Saha, M.M. Abu-Omar, Advances in 5-hydroxymethylfurfural production from biomass in biphasic solvents, Green Chem. 16 (2014) 24–38, <https://doi.org/10.1039/c3gc41324a>.
- [21] X. Zheng, X. Gu, Y. Ren, Z. Zhi, X. Lu, Production of 5-hydroxymethyl furfural and levulinic acid from lignocellulose in aqueous solution and different solvents, Biofuels, Bioprod. Biorefining. 10 (2016) 917–931, <https://doi.org/10.1002/bbb.1720>.
- [22] A.H. Motagamwala, W. Won, C. Sener, D.M. Alonso, C.T. Maravelias, J.A. Dumesic, Toward biomass-derived renewable plastics: production of 2,5-furandicarboxylic acid from fructose, Sci. Adv. 4 (2018) eaap9722, <https://doi.org/10.1126/sciadv.aap9722>.
- [23] B. Liu, K. Lv, J. Zhen, Z. Zhang, K. Deng, Selective aerobic oxidation of the biomass-derived precursor 5-hydroxymethylfurfural to 2,5-furandicarboxylic acid under mild conditions over a magnetic palladium nanocatalyst, Green Chem. 17 (2014) 1308–1317, <https://doi.org/10.1039/c4gc01833h>.
- [24] X. Zuo, P. Venkatasubramanian, D.H. Busch, B. Subramaniam, Optimization of Co/Mn/Br-catalyzed oxidation of 5-hydroxymethylfurfural to enhance 2,5-furandicarboxylic acid yield and minimize substrate burning, ACS Sustain. Chem. Eng. 4 (2016) 3659–3668, <https://doi.org/10.1021/acssuschemeng.6b00174>.
- [25] S.R. Kubota, K.S. Choi, Electrochemical oxidation of 5-hydroxymethylfurfural to 2,5-furandicarboxylic acid (Fdca) in acidic media enabling spontaneous fdca separation, ChemSusChem. 11 (2018) 2138–2145, <https://doi.org/10.1002/cssc.201800532>.
- [26] X. Wan, C. Zhou, J. Chen, W. Deng, Q. Zhang, Y. Yang, Y. Wang, Base-free aerobic oxidation of 5-hydroxymethyl-furfural to 2,5-furandicarboxylic acid in water catalyzed by functionalized carbon nanotube-supported au-pd alloy nanoparticles, ACS Catal. 4 (2014) 2175–2185, <https://doi.org/10.1021/cs5003096>.
- [27] Q. Wu, Y. He, H. Zhang, Z. Feng, Y. Wu, T. Wu, Photocatalytic selective oxidation of biomass-derived 5-hydroxymethylfurfural to 2,5-diformylfuran on metal-free g-C<sub>3</sub>N<sub>4</sub> under visible light irradiation, Mol. Catal. 436 (2017) 10–18, <https://doi.org/10.1016/j.mcat.2017.04.012>.
- [28] G. Lv, H. Wang, Y. Yang, T. Deng, C. Chen, Y. Zhu, X. Hou, Graphene oxide: a convenient metal-free carbocatalyst for facilitating aerobic oxidation of 5-Hydroxymethylfurfural into 2, 5-Diformylfuran, ACS Catal. 5 (2015) 5636–5646, <https://doi.org/10.1021/acscatal.5b01446>.
- [29] G. Lv, H. Wang, Y. Yang, X. Li, T. Deng, C. Chen, Y. Zhu, X. Hou, Aerobic selective oxidation of 5-hydroxymethyl-furfural over nitrogen-doped graphene materials with 2,2,6,6-tetramethylpiperidin-oxyl as co-catalyst, Catal. Sci. Technol. 6 (2016) 2377–2386, <https://doi.org/10.1039/C5CY01149C>.
- [30] B. Ma, Y. Wang, X. Guo, X. Tong, C. Liu, Y. Wang, X. Guo, Photocatalytic synthesis of 2,5-diformylfuran from 5-hydroxymethylfurfural or fructose over bimetallic Au-Ru nanoparticles supported on reduced graphene oxides, Appl. Catal. A Gen. 552 (2018) 70–76, <https://doi.org/10.1016/j.apcata.2018.01.002>.
- [31] Z. Yang, W. Qi, R. Su, Z. He, Selective synthesis of 2,5-Diformylfuran and 2,5-Furandicarboxylic acid from 5-Hydroxymethylfurfural and fructose catalyzed by magnetically separable catalysts, Energy Fuels 31 (2017) 533–541, <https://doi.org/10.1021/acs.energyfuels.6b02012>.
- [32] M.N. Kopylovich, A.P.C. Ribeiro, E.C.B.A. Alegria, N.M.R. Martins, L.M.D.R.S. Martins, A.J.L. Pombeiro, Catalytic oxidation of alcohols: recent advances, Adv. Organomet. Chem. 63 (2015) 91–174, <https://doi.org/10.1016/bs.adomc.2015.02.004>.
- [33] R.A. Sheldon, Recent advances in green catalytic oxidations of alcohols in aqueous media, Catal. Today 247 (2015) 4–13, <https://doi.org/10.1016/j.cattod.2014.08.024>.
- [34] L. Zhao, B. Zhang, X. Xiao, F.L. Gu, R.Q. Zhang, Roles of the active species involved in the photocatalytic oxidation of benzyl alcohol into benzaldehyde on TiO<sub>2</sub> under UV light: experimental and DFT studies, J. Mol. Catal. A Chem. 420 (2016) 82–87, <https://doi.org/10.1016/j.molcata.2016.03.012>.
- [35] A. Magdziarz, J.C. Colmenares, O. Chernyayeva, K. Kurzydłowski, J. Grzonka, Iron-containing titania photocatalyst prepared by the sonophotodeposition method for the oxidation of benzyl alcohol, ChemCatChem. 8 (2016) 536–539, <https://doi.org/10.1002/cctc.201501250>.
- [36] Y. Chen, H. Lim, Q. Tang, Y. Gao, T. Sun, Q. Yan, Y. Yang, Solvent-free aerobic oxidation of benzyl alcohol over Pd monometallic and Au-Pd bimetallic catalysts supported on SBA-16 mesoporous molecular sieves, Appl. Catal. A Gen. 380 (2010) 55–65, <https://doi.org/10.1016/j.apcata.2010.03.026>.
- [37] J.C. Colmenares, W. Ouyang, M. Ojeda, E. Kuna, O. Chernyayeva, D. Lisovytskiy, S. De, R. Luque, A.M. Balu, Mild ultrasound-assisted synthesis of TiO<sub>2</sub>supported on magnetic nanocomposites for selective photo-oxidation of benzyl alcohol, Appl. Catal. B Environ. 183 (2016) 107–112, <https://doi.org/10.1016/j.apcatb.2015.10.034>.
- [38] W. Ouyang, E. Kuna, A. Yezep, A. Balu, A. Romero, J. Colmenares, R. Luque, Mechanochemical synthesis of TiO<sub>2</sub> nanocomposites as photocatalysts for benzyl alcohol photo-oxidation, Nanomaterials 6 (2016) 93, <https://doi.org/10.3390/nano6050093>.
- [39] V. Augugliaro, L. Palmisano, Green oxidation of alcohols to carbonyl compounds by

- heterogeneous photocatalysis, *ChemSusChem* 3 (2010) 1135–1138, <https://doi.org/10.1002/cssc.201000156>.
- [40] K. Mullick, S. Biswas, A.M. Angeles-Boza, S.L. Suib, Heterogeneous mesoporous manganese oxide catalyst for aerobic and additive-free oxidative aromatization of N-heterocycles, *Chem. Commun.* 53 (2017) 2256–2259, <https://doi.org/10.1039/C6CC09095H>.
- [41] Z. Sibaib, F. Puleo, J.M. Garcia-Vargas, L. Retailleau, C. Descorme, L.F. Liotta, J.L. Valverde, S. Gil, A. Giroir-Fendler, Manganese oxide-based catalysts for toluene oxidation, *Appl. Catal. B Environ.* 209 (2017) 689–700, <https://doi.org/10.1016/j.apcatb.2017.03.042>.
- [42] M. Wiechen, L. Spiccia, Manganese oxides as efficient water oxidation catalysts, *ChemCatChem* 6 (2014) 439–441, <https://doi.org/10.1002/cctc.201300967>.
- [43] E. Hayashi, Y. Yamaguchi, K. Kamata, N. Tsunoda, Y. Kumagai, F. Oba, M. Hara, Effect of MnO<sub>2</sub> crystal structure on aerobic oxidation of 5-Hydroxymethylfurfural to 2,5-Furandicarboxylic acid, *J. Am. Chem. Soc.* 141 (2019) 899–900, <https://doi.org/10.1021/jacs.8b09917>.
- [44] Q. Liu, X. Duan, H. Sun, Y. Wang, M.O. Tade, S. Wang, Size-tailored porous spheres of manganese oxides for catalytic oxidation via peroxymonosulfate activation, *J. Phys. Chem. C* 120 (2016) 16871–16878, <https://doi.org/10.1021/acs.jpcc.6b05934>.
- [45] S.G. Babu, P. Karthik, M.C. John, S.K. Lakhera, M. Ashokkumar, J. Khim, B. Neppolian, Synergistic effect of sono-photocatalytic process for the degradation of organic pollutants using CuO-TiO<sub>2</sub>/rGO, *Ultrason. Sonochem.* 50 (2018) 218–223, <https://doi.org/10.1016/j.ultrsonch.2018.09.021>.
- [46] K.P. Vidya Lekshmi, S. Yesodharan, E.P. Yesodharan, MnO<sub>2</sub> efficiently removes indigo carmine dyes from polluted water, *Heliyon* 4 (2018), <https://doi.org/10.1016/j.heliyon.2018.e00897>.
- [47] H.S. Saroyan, S. Bele, D.A. Giannakoudakis, V.F. Samanidou, T.J. Bandosz, E.A. Delyianni, Degradation of endocrine disruptor, bisphenol-A, on a mixed oxidation state manganese oxide / modified graphite oxide composite : a role of carbonaceous phase, *J. Colloid Interface Sci.* 539 (2019) 516–524, <https://doi.org/10.1016/j.jcis.2018.12.088>.
- [48] B. Liu, Z. Zhang, K. Lv, K. Deng, H. Duan, Efficient aerobic oxidation of biomass-derived 5-hydroxymethylfurfural to 2,5-diformylfuran catalyzed by magnetic nanoparticle supported manganese oxide, *Appl. Catal. A Gen.* 472 (2014) 64–71, <https://doi.org/10.1016/j.apcata.2013.12.014>.
- [49] Z. Yuan, B. Liu, P. Zhou, Z. Zhang, Q. Chi, Aerobic oxidation of biomass-derived 5-hydroxymethylfurfural to 2,5-diformylfuran with cesium-doped manganese dioxide, *Catal. Sci. Technol.* 8 (2018) 4430–4439, <https://doi.org/10.1039/c8cy01246f>.
- [50] S. Biswas, B. Dutta, A. Mannodi-Kanakkithodi, R. Clarke, W. Song, R. Ramprasad, S.L. Suib, Heterogeneous mesoporous manganese/cobalt oxide catalysts for selective oxidation of 5-hydroxymethylfurfural to 2,5-diformylfuran, *Chem. Commun.* 53 (2017) 11751–11754, <https://doi.org/10.1039/C7CC06097A>.
- [51] H. Wang, C. Zhu, D. Li, Q. Liu, J. Tan, C. Wang, C. Cai, L. Ma, Recent advances in catalytic conversion of biomass to 5-hydroxymethylfurfural and 2,5-diformylfuran, *Renew. Sustain. Energy Rev.* 103 (2019) 227–247, <https://doi.org/10.1016/j.rser.2018.12.010>.
- [52] H. Zhang, Z. Feng, Y. Zhu, Y. Wu, T. Wu, Q. Wu, Y. He, H. Zhang, Z. Feng, Y. Wu, T. Wu, Photocatalytic selective oxidation of biomass-derived 5-hydroxymethylfurfural to 2,5-diformylfuran on WO<sub>3</sub>/g-C<sub>3</sub>N<sub>4</sub> composite under irradiation of visible light, *J. Photochem. Photobiol. A Chem.* 371 (2019) 1–9, <https://doi.org/10.1016/j.jphotochem.2018.10.044>.
- [53] M. Ilkaeva, I. Krivtsov, E.I. García-López, G. Marci, O. Khainakova, J.R. García, L. Palmisano, E. Díaz, S. Ordóñez, Selective photocatalytic oxidation of 5-hydroxymethylfurfural to 2,5-furandicarboxaldehyde by polymeric carbon nitride-hydrogen peroxide adduct, *J. Catal.* 359 (2018) 212–222, <https://doi.org/10.1016/j.jcat.2018.01.012>.
- [54] H. Zhang, Q. Wu, C. Guo, Y. Wu, T. Wu, Photocatalytic Selective Oxidation of 5-Hydroxymethylfurfural to 2,5-Diformylfuran over Nb<sub>2</sub>O<sub>5</sub> under visible light, *ACS Sustain. Chem. Eng.* 5 (2017) 3517–3523, <https://doi.org/10.1021/acssuschemeng.7b00231>.
- [55] L. Özcan, P. Yaşın, O. Alagöz, S. Yurdakal, Selective photoelectrocatalytic oxidation of 5-(hydroxymethyl)-2-furaldehyde in water by using Pt loaded nanotube structure of TiO<sub>2</sub> on Ti photoanodes, *Catal. Today* 281 (2017) 205–213, <https://doi.org/10.1016/j.cattod.2016.07.024>.
- [56] Y. Ma, S.G. Wang, M. Fan, W.X. Gong, B.Y. Gao, Characteristics and defluorination performance of granular activated carbons coated with manganese oxides, *J. Hazard. Mater.* 168 (2009) 1140–1146, <https://doi.org/10.1016/j.jhazmat.2009.02.145>.
- [57] M. Ramesh, H.S. Nagaraja, M.P. Rao, S. Anandan, N.M. Huang, Fabrication, characterization and catalytic activity of  $\alpha$ -MnO<sub>2</sub>nanowires for dye degradation of reactive black 5, *Mater. Lett.* 172 (2016) 85–89, <https://doi.org/10.1016/j.matlet.2016.02.076>.
- [58] L. Feng, Z. Xuan, H. Zhao, Y. Bai, J. Guo, C. Su, X. Chen, MnO<sub>2</sub> prepared by hydrothermal method and electrochemical performance as anode for lithium-ion battery, *Nanoscale Res. Lett.* 9 (2014) 290, <https://doi.org/10.1186/1556-276X-9-290>.
- [59] M. Thommes, K. Kaneko, A.V. Neimark, J.P. Olivier, F. Rodriguez-Reinoso, J. Rouquerol, K.S.W.W. Sing, Physisorption of gases, with special reference to the evaluation of surface area and pore size distribution (IUPAC Technical Report), *Pure Appl. Chem.* 87 (2015) 1051–1069, <https://doi.org/10.1515/pac-2014-1117>.
- [60] D.A. Giannakoudakis, F. Pearsall, M. Florent, J. Lombardi, S. O'Brien, T.J. Bandosz, Barium titanate perovskite nanoparticles as a photoreactive medium for chemical warfare agent detoxification, *J. Colloid Interface Sci.* 531 (2018) 233–244, <https://doi.org/10.1016/j.jcis.2018.07.053>.
- [61] D.A. Giannakoudakis, M. Jiang, T.J. Bandosz, Highly efficient air desulfurization on self-assembled bundles of copper hydroxide nanorods, *ACS Appl. Mater. Interfaces* 8 (2016) 31986–31994, <https://doi.org/10.1021/acsaami.6b10544>.
- [62] M. Florent, D.A. Giannakoudakis, R. Wallace, T.J. Bandosz, Mixed CuFe and ZnFe (hydr)oxides as reactive adsorbents of chemical warfare agent surrogates, *J. Hazard. Mater.* 329 (2017), <https://doi.org/10.1016/j.jhazmat.2017.01.036>.
- [63] J. Qu, L. Shi, C. He, F. Gao, B. Li, Q. Zhou, H. Hu, G. Shao, X. Wang, J. Qiu, Highly efficient synthesis of graphene/MnO<sub>2</sub> hybrids and their application for ultrafast oxidative decomposition of methylene blue, *Carbon N. Y.* 66 (2014) 485–492, <https://doi.org/10.1016/j.carbon.2013.09.025>.
- [64] K. Terayama, M. Ikeda, Study on thermal decomposition of MnO<sub>2</sub> and Mn<sub>2</sub>O<sub>3</sub> by thermal analysis, *Trans. Jpn. Inst. Met.* 24 (1983) 754–758, <https://doi.org/10.2320/matertrans1960.24.754>.
- [65] F. Vendruscolo, M.J. Rossi, W. Schmidell, J.L. Ninow, Determination of oxygen solubility in liquid media, *ISRN Chem. Eng.* 2012 (2012) 1–5, <https://doi.org/10.5402/2012/601458>.
- [66] R.G. Wetzel, G.E. Likens, Dissolved oxygen, *Limnol. Anal.* 49 (2000) 73–84, [https://doi.org/10.1007/978-1-4757-3250-4\\_6](https://doi.org/10.1007/978-1-4757-3250-4_6).
- [67] C. Franco, J. Olmsted, Photochemical determination of the solubility of oxygen in various media, *Talanta* 37 (1990) 905–909, [https://doi.org/10.1016/0039-9140\(90\)80251-A](https://doi.org/10.1016/0039-9140(90)80251-A).
- [68] Q. Li, C. Batchelor-Mcauley, N.S. Lawrence, R.S. Hartshorne, R.G. Compton, Anomalous solubility of oxygen in acetonitrile/water mixture containing tetra-n-butylammonium perchlorate supporting electrolyte; the solubility and diffusion coefficient of oxygen in anhydrous acetonitrile and aqueous mixtures, *J. Electroanal. Chem.* 688 (2013) 328–335, <https://doi.org/10.1016/j.jelechem.2012.07.039>.
- [69] J.M. Achord, C.L. Hussey, Determination of dissolved oxygen in nonaqueous electrochemical solvents, *Anal. Chem.* 52 (1980) 601–602, <https://doi.org/10.1021/ac50053a061>.
- [70] V. Nair, M.J. Muñoz-Batista, M. Fernández-García, R. Luque, J.C. Colmenares, Thermo-photocatalysis: environmental and energy applications, *ChemSusChem* (2019) 2098–2116, <https://doi.org/10.1002/cssc.201900175>.
- [71] Z. Mo, H. Xu, Z. Chen, X. She, Y. Song, J. Lian, X. Zhu, P. Yan, Y. Lei, S. Yuan, H. Li, Construction of MnO<sub>2</sub>/Monolayer g-C<sub>3</sub>N<sub>4</sub> with Mn vacancies for Z-scheme overall water splitting, *Appl. Catal. B Environ.* 241 (2018) 452–460, <https://doi.org/10.1016/j.apcatb.2018.08.073>.
- [72] J. Nie, H. Liu, Efficient aerobic oxidation of 5-hydroxymethylfurfural to 2,5-diformylfuran on manganese oxide catalysts, *J. Catal.* 316 (2014) 57–66, <https://doi.org/10.1016/j.jcat.2014.05.003>.
- [73] C. Megias-Sayago, K. Chakarova, A. Penkova, A. Lolli, S. Ivanova, S. Albonetti, F. Cavani, J.A. Odriozola, Understanding the role of the acid sites in 5-Hydroxymethylfurfural Oxidation to 2,5-Furandicarboxylic acid reaction over gold catalysts: surface investigation on Ce<sub>x</sub>Zr<sub>1-x</sub>O<sub>2</sub> Compounds, *ACS Catal.* (2018) 11154–11164, <https://doi.org/10.1021/acscatal.8b02522>.
- [74] Bhushan N. Zope, David D. Hibbitts, Matthew Neurock, Robert J. Davis, Reactivity of the Gold/Water interface during selective oxidation catalysis, *Science* (80) 330 (2010) 74–78, <https://doi.org/10.1126/science.1195055>.
- [75] D.A. Giannakoudakis, J.K. Mitchell, T.J. Bandosz, Reactive adsorption of mustard gas surrogate on zirconium (hydr)oxide/graphite oxide composites: the role of surface and chemical features, *J. Mater. Chem. A* 4 (2016) 1008–1019, <https://doi.org/10.1039/C5TA09234E>.
- [76] D.A. Giannakoudakis, M. Florent, R. Wallace, J. Secor, C. Karwacki, T.J. Bandosz, Zinc peroxide nanoparticles: surface, chemical and optical properties and the effect of thermal treatment on the detoxification of mustard gas, *Appl. Catal. B Environ.* 226 (2018) 429–440, <https://doi.org/10.1016/j.apcatb.2017.12.068>.
- [77] S.E. Davis, B.N. Zope, R.J. Davis, On the mechanism of selective oxidation of 5-hydroxymethylfurfural to 2,5-furandicarboxylic acid over supported Pt and Au catalysts, *Green Chem.* 14 (2012) 143–147, <https://doi.org/10.1039/c1gc16074e>.